Applied Catalysis A: General 495 (2015) 84–91

Contents lists available at ScienceDirect

Applied Catalysis A: General

journal homepage: www.elsevier.com/locate/apcata

Glycerol dehydration catalyzed by MWW zeolites and the changes in the catalyst deactivation caused by porosity modification

Mariana V. Rodrigues[a], Charito Vignatti[b], Teresita Garetto[b], Sandra H. Pulcinelli[a], Celso V. Santilli[a], Leandro Martins[a,*]

[a] Instituto de Química de Araraquara (UNESP), Rua Prof. Francisco Degni 55, 14800-900 Araraquara, SP, Brazil
[b] Catalysis Science and Engineering Research Group (GICIC) – Instituto de Investigaciones en Catalisis y Petroquímica (INCAPE), Santiago del Estero 2654, Santa Fe, Argentina

ARTICLE INFO

Article history:
Received 15 December 2014
Received in revised form 4 February 2015
Accepted 7 February 2015
Available online 16 February 2015

Keywords:
MWW zeolites
Glycerol dehydration
Deactivation
Pillarization
Delamination

ABSTRACT

Members of the layered MWW family, including microporous MCM-22, pillared MCM-36 and delaminated ITQ-2 zeolites, were used as catalysts for the gas phase dehydration of glycerol. The chemical, structural and surface properties of the catalysts were characterized by X-ray diffraction, N_2 adsorption–desorption isotherms, SEM, TEM, NH_3-TPD and pyridine chemisorption followed by IR spectroscopy. The results clearly showed that the modified zeolites with designed mesopore structure enabled rapid diffusion and consequently improved the glycerol conversion. Characterization of the acid sites revealed that the relative abundance of Brønsted and Lewis acid sites influenced the efficiency of the catalysis performed by these materials. ^{13}C NMR spectra of the spent catalysts confirmed that differences in the nature and amount of carbonaceous deposits are related to the pore structures of the catalysts, with greater formation of polyaromatic compounds inside zeolite pores, while polyglycols are preferentially formed at the external surfaces of the MCM-36 and ITQ-2 zeolites, as expected for the more exposed sheets.

© 2015 Elsevier B.V. All rights reserved.

1. Introduction

Renewable fuels are increasingly in demand due to the depletion of fossil fuel resources combined with greater global fuel consumption. Biodiesel, which production grows every year [1], is an attractive option, but 1 kg of glycerol is generated as a byproduct for every 9 kg of biodiesel manufactured. This feature results in a substantial availability of glycerol as a raw material for industrial purposes, so that the effective use of glycerol is essential to improve the profitability of biodiesel production [2]. The glycerol molecule shows in each carbon a functional group, thus, several applications are possible to chemical industries [3].

The conversion of glycerol can be achieved using oxidation, reforming, hydrogenolysis, esterification and etherification. Another method is the dual intramolecular dehydration of glycerol to acrolein, which is an intermediate in the production of acrylic acid, widely used in the manufacture of adhesives, paints, plastics, and super-absorbents [4–6].

Dehydration of glycerol in the gas phase is advantageous, because the adjustment of parameters such as temperature and contact time enables the tailoring of the conversion and the selectivity [6]. Many solid catalysts have been employed in this reaction and it has been found that catalytic conversion and stability depend on characteristics of the material including the strength, distribution, and type (Brønsted or Lewis) of acid sites, as well as the pore size and access of reactants to the internal active sites. Mesoporous catalysts show better performance compared to purely microporous ones. Sorption of reactants at weak Lewis acid sites favors the single intramolecular dehydration of glycerol to hydroxyacetone, while strong or moderate Brønsted acid sites are more efficient for the production of acrolein. A negative aspect of the Brønsted sites is that they not only favor the production of acrolein, but also of carbonaceous deposits that are responsible for strong catalyst deactivation by deposition of non-reactive compounds that obstruct the pores and cover the active sites [6,7]. This is a major problem that needs to be overcome in catalysts design.

Acid catalysts that have been tested for gas-phase glycerol dehydration at temperatures ranging from 275 to 350 °C include TiO_2, SiO_2/Al_2O_3, and pure Al_2O_3. However, these materials do not provide selectivity toward acrolein. Improved selectivity has been achieved using Nb_2O_5, WO_3/ZrO_2, metal phosphates (Al_2O_3–PO_4

* Corresponding author. Tel.: +55 16 3301 9705.
E-mail address: leandro@iq.unesp.br (L. Martins).

http://dx.doi.org/10.1016/j.apcata.2015.02.010
0926-860X/© 2015 Elsevier B.V. All rights reserved.

and TiO_2–PO_4), and heteropolyacids, although the catalysts showed poor stability due to the formation of coke [4,6].

Zeolites have attracted attention because of their stability under a range of catalytic conditions, together with the selectivity provided by their pore systems and the strong Brønsted acid sites that are produced by substitution of silicon by aluminum atoms in the framework. Nevertheless, a microporous framework is unfavorable because it hinders the access of bulky molecules, and the diffusion and mass transport of reactants and products are restricted [8–10]. Furthermore, the deposition of coke readily blocks the micropores, so that the internal acid sites become inaccessible and useless.

MCM-22 zeolite is an interesting structure by having MWW framework with some particularities. This was the first lamellar zeolite to be synthesized in 1990, and has a unique pore structure that enables its use in a variety of different applications. Layered zeolites provide a combination of the chemical characteristics of conventional microporous zeolites, together with access to inner active sites, which makes them attractive for use in catalysis [11–14]. The main distinct aspect between conventional and layered zeolites comes from the fact that adsorption and catalysis in lamellar zeolites occur almost expressly at the surface and not inside pores [15]. Moreover comparing 2D zeolites and layered material in general, zeolites exhibit an advantage in porosity since there are pores in own layers [16].

The lamellar precursor MCM-22 can be pillared and delaminated under suitable conditions giving rise to the MCM-36 and ITQ-2 zeolites, respectively. The three zeolites have different porosities and belong to the same MWW framework family [8,17–20]. MCM-36 is a pillared layered structure built of inorganic layers with inorganic pillars appended on both sides of the sheets. The pillars preserve the interlayer separation, while the void space created after removal of the swelling agent produces mesopores. The pillared zeolite has an advantage due to its mesopores distribution which facilitates the catalysis with large molecules, besides keeping MWW sheets physico-chemical characteristics. Delaminated ITQ-2 consists of thin MWW sheets of approximately 2.5 nm thick, showing an extremely high external surface area combined with an acidity and hydrothermal stability common to zeolites, without a long-range order. The random spatial distribution of sheets yields aggregation mesopores between the layers. This mesoporosity is very interesting for reactions that involve large molecules [21,22].

In this study, we compare and discuss the gas-phase dehydration of glycerol to acrolein catalyzed by an assemblage of lamellar MWW zeolites. The effect of catalyst porosity on the distribution of products, on the control of diffusion constraints and accessibility to the acid sites and, finally, on the catalyst deactivation and coke speciation is shown.

2. Experimental

2.1. Synthesis of the MCM-22P zeolite precursor

The procedure used to synthesize the MCM-22 precursor (denoted MCM-22P) was adapted from Ref. [23]. The synthesis mixture was prepared by adding 0.531 g of NaOH to 35.8 g of deionized water under constant stirring until complete dissolution, and then by adding 0.425 g of sodium aluminate (Sigma–Aldrich). After this, 6.58 g of the organic template, hexamethylenimine (HMI, Sigma–Aldrich) was added drop by drop under constant vigorous mechanical stirring at 50 °C for 30 min. Addition of 6.65 g of fumed silica (200 m^2/g, Sigma–Aldrich) was then performed slowly under the same conditions of temperature and stirring, allowing 30 min for complete homogenization. The final mole composition of the synthesis mixture was 50 SiO_2:1 $NaAl_2O_3$:6 NaOH:30 HMI:900 H_2O. This mixture was transferred to a Teflon-lined autoclave and heated at 150 °C for 5 days under static and autogenous conditions. The precipitated product was washed with acidified water (0.1 wt.% acetic acid) until pH 7.0, and then dried at 100 °C for 1 day prior to production of the MCM-22 zeolite. For the other zeolites (ITQ-2 and MCM-36), the MCM-22P precursor was not dried to avoid any partial condensation of the layers that might hinder the subsequent swelling process.

2.2. Synthesis of the MCM-22 zeolite

The dried MCM-22P zeolite was calcined at 550 °C for 3 h, using a heating rate of 2 °C/min, resulting in the formation of MCM-22 zeolite.

2.3. Synthesis of the MCM-36 and ITQ-2 zeolites

Prior to the synthesis of MCM-36 and ITQ-2, the wet MCM-22P zeolite sheets were swollen using a procedure based on Ref. [18]. Briefly, 5.0 g of MCM-22P and 28.2 g of CTABr (hexadecyltrimethylammonium bromide, Sigma–Aldrich) were mixed with 97.4 g of deionized water, followed by addition of 61.2 g of a 20 wt.% solution of TPAOH (tetrapropylammonium hydroxide, Sigma–Aldrich). The mixture was kept under reflux at 80 °C and pH 12.3 for 24 h.

The pillaring procedure used to produce MCM-36 was adapted from Refs. [24,25]. The swollen MCM-22P zeolite (MCM-22S) was gradually dried at 25 °C for 7 days. Mild conditions were used in order to avoid condensation of the layers. A mass of 3.0 g of the dried zeolite was then mixed with 15 g of TEOS (tetraethyl orthosilicate, Sigma–Aldrich) and refluxed at 80 °C for 24 h under nitrogen atmosphere and continuous stirring. The resulting material was dried at 25 °C and then hydrolyzed at 80 °C for 24 h with an amount of water corresponding to ten times the mass of zeolite. During the hydrolysis, the pH was adjusted to 8 with a concentrated NaOH solution. The solid was filtered, washed, dried, and calcined under air flow at 450 °C for 3 h and then at 550 °C for 6 h, using heating rates of 2 °C/min.

For the production of ITQ-2 by delamination of swollen MCM-22P, the balloon flask used for the swelling procedure was immersed in an ultrasonic bath at 50 °C for 2 h. After the layers had been forced apart, hydrochloric acid was added until the pH reached 2. The mixture was then washed, centrifuged, and dried at 100 °C for 12 h. The resulting material was calcined at 550 °C for 3 h, using a heating rate of 2 °C/min [26,27].

The synthesized zeolites were converted in the H-form by three consecutive ion exchanges of 1 g of zeolite in 50 mL of 0.1 mol/L NH_4NO_3 solution at ambient temperature for 3 h and subsequent calcination at 500 °C (heating rate of 5 °C/min) for 2 h under air atmosphere.

2.4. Characterization

The solid crystalline structures were analyzed by X-ray diffraction (XRD) using a Siemens D5000 diffractometer and Cu Kα radiation selected by a curved graphite monochromator. Data were collected in a 2θ range from 2° to 40°, using a step size of 0.01° and a counting time of 1 s.

The crystal size and morphology were examined by scanning electron microscopy (SEM) performed using a Philips FEG XL 30 instrument. The samples were previously deposited in aluminum sample holders and sputtered with gold. Transmission electron microscopy (TEM) analyses were performed using a JEOL 3010 microscope operating at 300 kV in high-resolution mode. The images were acquired for the layered zeolite crystals supported on a copper grid.

The chemical compositions of the samples were determined by atomic absorption spectroscopy (Model 240FS, Agilent).

The samples were characterized by solid-state ^{27}Al NMR. The spectra were recorded using a Varian INOVA 500 spectrometer equipped with a 4 mm probe at spinning rate of 14 kHz. The ^{27}Al chemical shifts were referenced to a 1.0 mol/L $Al(NO_3)_3$ aqueous solution. The experimental conditions were operating frequency of 130.07 MHz, acquisition time of 0.0164 ms, pulse width of 1.1 ms, and recycle delay of 5 s. For each spectrum 256 scans were acquired.

The textural characterization of the solids was done by nitrogen adsorption–desorption isotherms obtained at liquid nitrogen temperature, with a relative pressure interval of between 0.001 and 0.998, using a Micromeritics ASAP 2010 instrument. Prior to the measurements, the samples were evacuated at 200 °C for 12 h. Micropore volume was determined by *t*-plot method. The Barrett–Joyner–Halenda (BJH) method was used to determine the mesopore size distributions. The quantification of pore volume for the different families of mesopores (aggregation pores and mesopores formed by pillarization) was calculated using the BJH method in combination with the Kelvin (Eq. (1)) and Harkins–Jura equations (Eq. (2)). These two equations were used to correlate the pore size distribution in BJH plots with the P/P_0 values of the nitrogen desorption branch of the isotherms, and therefore to determine the corresponding adsorbed nitrogen volume in normal conditions of pressure and temperature. The used liquid nitrogen parameters at 77 K were surface tension γ of 8.85×10^{-3} N/m, mole volume V_L of 3.46×10^{-5} m^3/mol and density ρ of 809 kg/m^3. The values of pore radius r_p and thickness t of adsorbed nitrogen were given in nm.

$$r_p = -\frac{2 \cdot \gamma \cdot V_L}{\ln(P/P_0) \cdot RT} \times 10^9 + t(P/P_0); \quad (1)$$

$$t = \sqrt{\frac{13.99}{0.034 - \log\ (P/P_0)}} \times 10^{-1} \quad (2)$$

Acid site densities were determined by temperature-programmed desorption of NH_3 (NH_3-TPD). A mass of 150 mg of sample was previously treated in He (60 mL/min) at 200 °C for 1 h, and then cooled to 100 °C. At this temperature, the samples were exposed to a flow of 1% of NH_3 in He (60 mL/min) for 1 h, so that the surface became saturated. The physisorbed ammonia was then removed under He flow for 1 h, before increasing the temperature to 700 °C at 10 °C/min. The NH_3 concentration in the effluent was analyzed by mass spectrometry (OmniStar Balzers Instruments).

The nature of the surface acid sites was determined by Fourier transform infrared spectroscopy (FTIR), using a Shimadzu Prestige 21 spectrophotometer and pyridine as the probe molecule. The spectral resolution was 4 cm^{-1}, and 40 scans were accumulated. Sample wafers (diameter = 25 mm) were performed by pressing 20 mg of the catalyst at 1.5 t/cm^2. All the samples were firstly degassed at 25 °C and 0.013 Pa for 30 min. Pyridine (2 μL) was introduced at room temperature, and the zeolites were exposed to the pyridine vapor for 5 min. Data were obtained after admission of pyridine, desorption at room temperature, and sequential evacuation at room temperature and then at 150, 300, and 450 °C. The spectra were always recorded at room temperature, with subtraction of the background spectrum previously recorded. The relative contributions of Lewis and Brønsted acid sites after the evacuation of pyridine were obtained by integration of the bands at 1440 cm^{-1} (Lewis sites) and 1540 cm^{-1} (Brønsted sites). The relative concentration $c_{Brønsted}/c_{Lewis}$ (Eq. (3)) of both acid sites was determined by means of the Beer–Lambert Law $A = \varepsilon \times c \times T$, where A stands for the integrated absorption peak area, ε is the Emeis molar extinction factor (1.67 cm/μmol for band at 1540 cm^{-1} and 2.22 cm/μmol for band at 1450 cm^{-1}), c is the concentration of sites in μmol/dm^3 and T the thickness of the sample in cm [28].

$$\frac{c_{Brø\,nsted}}{c_{Lewis}} = \frac{A_{1540\,cm^{-1}}}{A_{1450\,cm^{-1}}} \times \frac{T_{1450\,cm^{-1}}}{T_{1540\,cm^{-1}}} \times \frac{\varepsilon_{1450\,cm^{-1}}}{\varepsilon_{1540\,cm^{-1}}} \quad (3)$$

Thermogravimetric analyses of the used catalysts after the reaction were carried out under air flow (100 mL/min), using a TA SDT Q600 TGA/DSC thermobalance. The temperature range was 30–1000 °C and the heating rate 10 °C/min.

The spent and coked catalysts were characterized by ^{13}C nuclear magnetic resonance (CP MAS NMR), using a Bruker Avance III 400 MHz WB instrument equipped with a 4 mm probe and operated with a rotor spinning rate of 12 kHz. The catalyst samples were placed into a zirconia rotor of 4 mm outer diameter. All the rotors were filled with the same volume of sample. The ^{13}C NMR spectra were compared assuming the same bulk density for each sample and that the ^{13}C signal was proportional to the amount of coke deposited in the catalyst. The experimental conditions were a frequency of 100.61 kHz, pulse width of 3.8 ms and contact time of 2000 ms.

2.5. Glycerol dehydration

The catalytic dehydration of glycerol was carried out in the gas phase at 320 °C, at atmospheric pressure, in a continuous-flow glass fixed-bed reactor. Prior to the catalytic tests, 150 mg of the acid zeolite was heated to 320 °C under nitrogen flow of 15 mL/min and kept at this temperature for 15 min. Glycerol was used as received (99 wt.%, Sigma–Aldrich). A 10 wt.% glycerol solution in water was supplied at 0.05 mL/min through a heated line, controlled by a positive displacement pump (KD Scientific). Nitrogen was used as the carrier gas to ensure that the reactants and products formed during the reaction were efficiently transported to the gas–liquid separator kept at 1 °C by means of an ultra-low refrigerated circulator. The products collected in the gas–liquid separator were analyzed using a gas chromatograph (GC-2014, Shimadzu) equipped with a capillary column (Rtx-1, 30 m, 0.32 mm, 1 μm) and a FID detector. Before each injection, a known mass of n-butanol was added as an internal standard. The analyses were performed in triplicate. The quantification of all liquid products was done by comparison with an assembled calibration curve and afterwards used to calculate the carbon balance $(C_{out}/C_{in}) \times 100$. A carbon balance of 100 means that unconverted glycerol and all liquid products are outflowing the reactor. A carbon balance less than 100 means that heavy products are being kept adsorbed on the catalyst surface or decomposed as CO and CO_2.

The conversion of glycerol ($X_{glycerol}$) and the product selectivity (S) were calculated according to Eqs. (4) and (5), respectively, where n_{Gl}^{inlet} and n_{Gl}^{outlet} are the inlet and outlet mole flows of glycerol (mol/min), n_i is the mole flow of products i (mol/min), $Z_{Gl} = 3$ (the number of carbon atoms in the glycerol molecule), and Z_i represents the number of carbon atoms in the products [29].

$$X_{glycerol}\,(\%) = \frac{n_{Gl}^{inlet} - n_{Gl}^{outlet}}{n_{Gl}^{inlet}} \times 100; \quad (4)$$

$$S\,(\%) = \frac{n_i}{n_{Gl}^{inlet} - n_{Gl}^{outlet}} \times \frac{Z_i}{Z_{Gl}} \times 100 \quad (5)$$

The relative deactivation of the catalysts given in Eq. (6) was calculated considering X_0 and X, which are the glycerol conversions extrapolated at time zero and after 6 h of reaction, respectively.

$$D\ (\%) = \frac{X_0 - X}{X_0} \times 100 \quad (6)$$

3. Results and discussion

3.1. Textural characteristics of the zeolites

The X-ray powder diffraction analysis of the MCM-22P precursor material in Fig. 1 revealed patterns characteristic of the MWW

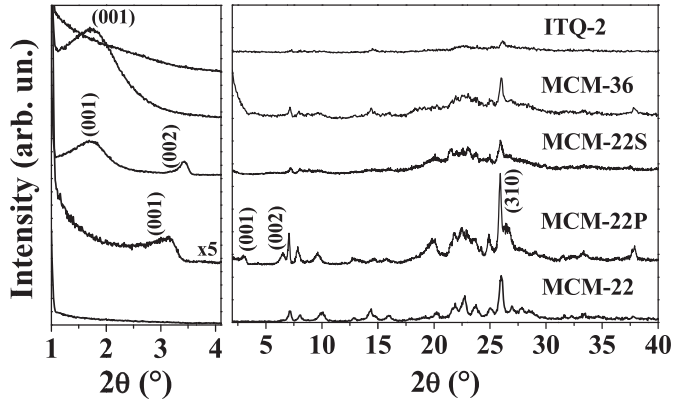

Fig. 1. X-ray powder diffraction patterns of the synthesized zeolites.

topology, notably peaks at 2θ of 26.3°, for (3 1 0), and in the range 3–7°, for (0 0 1) and (0 0 2), which are related to the separation between the zeolite sheets along the *c*-axis. The (0 0 2) peak at $2\theta = 6.4°$ was shifted to $2\theta = 7.1°$ after calcination, due to condensation of the sheets (interlayer distance decreases from 1.37 to 1.24 nm). The X-ray measurement at 2θ of 1.2–4° shows the shifted (0 0 1) and (0 0 2) peaks due to the increase of distance between sheets. For the MCM-22S sample, the (0 0 2) interlayer distance corresponds to 2.52 nm. Broader and less intense peaks were obtained for the alkali-treated MCM-22S zeolite, due to reductions in the particle size and layer thickness, partial delamination of the layers, or slight deviations of the layer orientation in the *c*-axis in the presence of CTABr. The decrease in the apparent crystallinity of the zeolite was due to mismatch between the positions of the silanol groups on each MWW layer. The MCM-36 material showed a very broad (0 0 1) peak at $2\theta = 1$–2°, indicating the formation of mesopores between columns of silica condensed in the interlayer region of the zeolite. The XRD pattern of ITQ-2 showed a general decrease in intensity, and severe broadening of the peaks. The 0 0 1 peaks characteristics of MWW structure does not appear in ITQ-2, consistent with the reduction of long-range order as the proposed structure of delaminated layers randomly orientated [21–23].

The loss of crystallinity, caused by severe exfoliation during the alkaline treatment, was also observed in the SEM images of ITQ-2, which revealed irregular shapes that did not resemble the rounded agglomerates of layers found for MCM-22 (Fig. 2). The organization of the layers was visualized by high-resolution TEM. A group of stacked 10 nm thick layers, with long-range order along the *c*-axis, was observed for MCM-22, while ITQ-2 showed a single assembly of layers with a narrow *c*-axis dimension.

The nitrogen adsorption and desorption isotherms provided evidences of substantial differences between MCM-22, MCM-36, and ITQ-2 zeolites (Fig. 3A). The MCM-22 material presented a type I isotherm due to its purely microporous structure, while the other zeolites showed a mixture of type I and type IV isotherms. The isotherm for MCM-36 showed a hysteresis loop corresponding to capillary condensation, indicating the successful formation of mesopores after swelling and subsequent insertion of polymeric silica pillars. Despite the exfoliation process led to undetectable micropore volume by *t*-plot method (n.d. in Table 1), the isotherm for ITQ-2 had the micropore fingerprint for low P/P_0 values. Some micropores still remained after the delamination process, with an H3-shaped hysteresis loop confirming the presence of slit-shaped pores related to the non-parallel packing of the layers in the material.

Although the MCM-22 sample was essentially microporous, only a small volume of pores was detected because of the densely packed layers. The results shown in Fig. 3A clearly indicated that all the samples possessed a system of pores that started to fill up at very low pressure, in the region of $P/P_0 \cong 1 \times 10^{-3}$. The micropore family ($V_1$ in Table 1 for pores lower than 2 nm) was not observed in the BJH distribution of Fig. 3B, due to the detection limit of the capillary condensation model, and consequently the purely microporous MCM-22 showed no pore distribution. Despite the significant nitrogen adsorption at low P/P_0, the micropore volume could not be determined by the *t*-plot method for MCM-36 and ITQ-2 due to the combination of two adsorption events, namely the low micropore volume of exfoliated layers and great interference of multilayer adsorption of nitrogen on the layers of zeolites in this region of the isotherm.

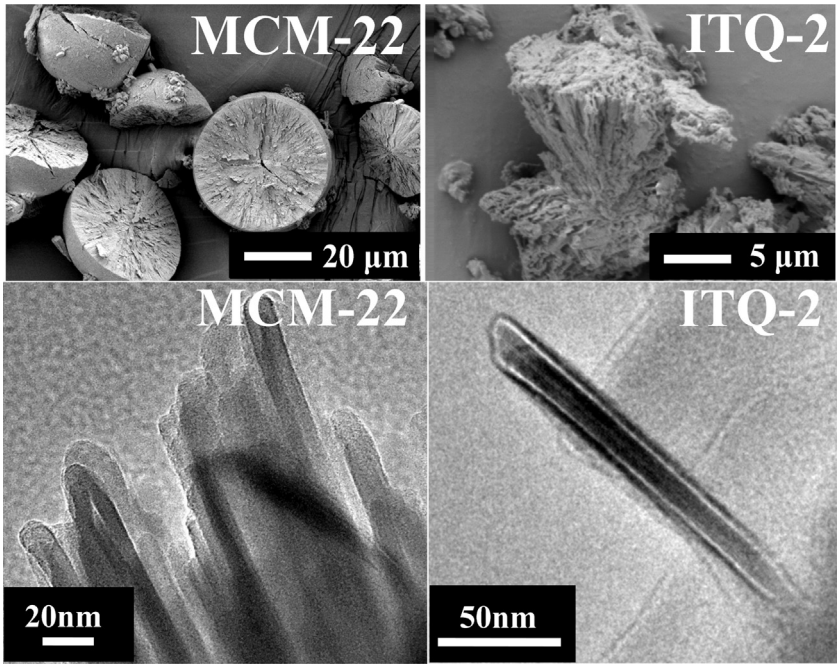

Fig. 2. SEM (top) and TEM (bottom) images of the MCM-22 and ITQ-2 zeolites.

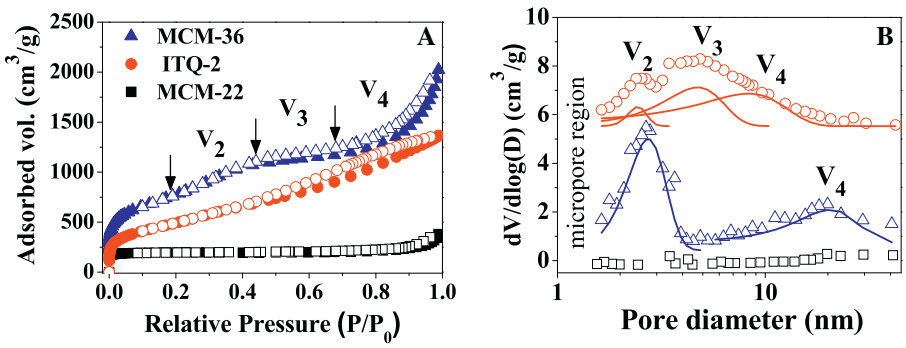

Fig. 3. (A) Nitrogen adsorption and desorption isotherms (filled and empty points correspond to nitrogen adsorption and desorption, respectively) and (B) BJH pore size distribution.

The BJH pore size distribution obtained from the desorption branch of the isotherms confirmed the creation of different families of pores in the samples (Fig. 3B). A broad distribution of pores was observed for ITQ-2 as a consequence of contribution of mesopores from different families, namely V_2, V_3 and V_4. The less intense V_2 type in ITQ-2 corresponds to layers produced in the first steps of an ill exfoliation process. The very broad V_3 and V_4 mesopores correspond to slit-like shaped pores created by indiscriminate aggregation of layers. In the case of MCM-36, the pores belonging to V_2 are generate by pillaring process due to silica insertion between layers and a less intense V_4 peak arises due to a partial exfoliation during pillaring or some interstitial holes among the particles [30].

3.2. Acidic characteristics of the zeolites

The acid properties of the samples, based on the nature and strength of acidic sites, were evaluated by TPD of NH_3 and FTIR analysis of adsorbed pyridine according to procedure described in a previous publication [29]. The NH_3-TPD curves (Fig. 4A) revealed two broad regions of ammonia desorption, one located at 200–300 °C, related to ammonia molecules chemisorbed on weak acid sites, and another at 400–600 °C, corresponding to ammonia adsorbed on stronger acid sites. The amount of chemisorbed ammonia was substantially lower after the pillaring and delamination procedures, due to a decrease in Brønsted acid species, caused by the loss of framework aluminum in swollen, pillaring and delamination process, unfortunately this loss in acidity is common in modified zeolites [31]. The chemisorption of ammonia was the lowest for the alumina reference material, which presented a very low and broad peak, in agreement with the weak nature of Lewis acid sites.

The presence of Brønsted and Lewis acid sites was evaluated from the results of pyridine FTIR analysis in the range of 1400–1700 cm^{-1} (Fig. 4B). A band near 1540 cm^{-1} was related to the formation of pyridinium cations (PyH^+), reflecting the presence of Brønsted acid sites, while a band centered at 1450 cm^{-1} corresponded to pyridine chemisorbed on Lewis acid sites (Py-L) [18]. The highest PyH^+/Py-L ratio (1.6) was obtained for the parent MCM-22 zeolite, suggesting that this material contained a greater number of Brønsted acid sites compared to the modified zeolites.

The presence of Brønsted acid sites is directly related to the aluminum content of the zeolite framework. The quantification of aluminum atoms on the basis of framework and extra-framework Si/Al mole ratio is therefore fundamental for understanding the influence of composition on zeolite acidity. Fig. 4C shows the ^{27}Al NMR spectra of all the samples with a main peak at chemical shift around 54 ppm (Td2) and a shoulder at 50 ppm (Td1) due to tetrahedrally coordinated aluminum in the framework of the hydrated zeolites. The differences in chemical shifts between the aluminum Td1 and Td2 were generated because each one was in a different crystallographic T sites. This non-random aluminum distribution behavior was already observed in other frameworks [32]. In the case of the alkali-treated zeolites (MCM-36 and ITQ-2) this peak was slightly broadened as a consequence of distortion of the tetrahedral arrangement.

The peaks related to the families of penta- and hexacoordinated aluminum species, usually present at around 30 ppm and in the range −10 to 0 ppm, respectively, are generally assigned to indefinite polymeric oxyhydroxy aluminum aggregates or to ionic particles that might act as charge balancing cations in the zeolite structure [29,33]. A peak at 30 ppm and a small shoulder at −10 ppm were observed for MCM-36 and ITQ-2, but not for MCM-22, confirming that the alkaline treatment affected the distribution of aluminum species and consequently, also affected the acidity. The relative intensities of the peaks corresponding to diverse aluminum species enabled approximate calculation of the framework Si/Al ratios. Table 1 compares the global silicon to aluminum mole ratio determined by atomic absorption spectroscopy and the framework mole ratio described by ^{27}Al NMR. The MWW framework chemical composition was affected by the

Table 1
Textural properties and chemical composition of lamellar MWW zeolites.

Samples	Si/Al-global[a]	Si/Al-framework[b]	Micropores[c]		Mesopores[d]		V total at P/P_0 0.99 (mL/g)
			V_1 (mL/g) <2 nm (P/P_0 < 0.19)	V_2 (mL/g) 2–3.5 nm (0.19 < P/P_0 < 0.44)	V_3 (mL/g) 3.5–6.5 nm (0.44 < P/P_0 < 0.67)	V_4 (mL/g) >6.5 nm (P/P_0 > 0.67)	
MCM-22	28	35	0.22	0	0	0	0.54
MCM-36	27	31	n.d.	0.53	0.20	1.21	2.39
ITQ-2	41	50	n.d.	0.34	0.48	0.51	2.09

[a] Global silicon to aluminum mole ratio.
[b] Framework silicon to aluminum mole ratio estimated from deconvolution of ^{27}Al NMR spectra.
[c] Volume of micropores calculated by the t-plot method.
[d] Volume of mesopores were determined considering the differences of adsorbed nitrogen volume given by arrows in Fig. 3A; the arrows position were determined with the aid of Eqs. (1) and (2).

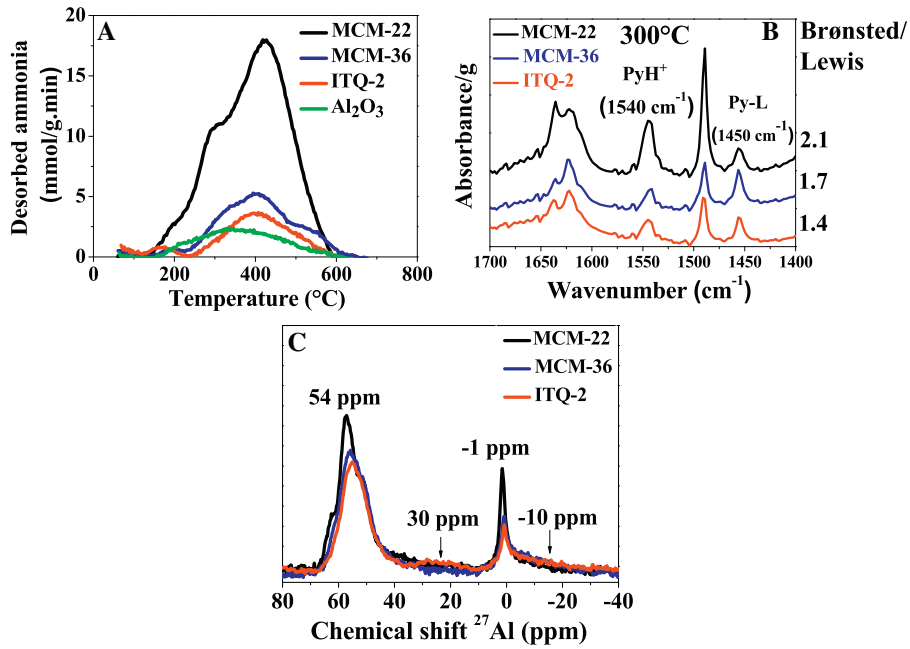

Fig. 4. Temperature-programmed desorption profiles of adsorbed ammonia (A), IR spectra of adsorbed pyridine after desorbing weakly bounded species at 300 °C (B), and ^{27}Al NMR spectra of the zeolites (C).

alkaline treatment after swelling, pillaring, and delamination. The main cause of the low acidity in modified zeolites is the difference between framework Si/Al ratio, *i.e.* the loss of tetrahedral aluminum atoms.

3.3. Glycerol dehydration catalyzed by MWW zeolites and the changes in the catalyst deactivation caused by porosity modification

The catalytic conversion of the lamellar MWW zeolites was investigated for the glycerol dehydration reaction, which can cause rapid catalyst deactivation due to the deposition of non-volatile carbonaceous byproducts on the catalyst surface. As expected, the lifetime of the catalyst during conversion of glycerol on the modified zeolites was longer, compared to the purely microporous MCM-22 zeolite (Fig. 5), despite the loss of Brønsted acid sites in modification procedures. This enhanced conversion in modified zeolites could be explained by the great accessibility of active sites located at the micro-mesopore surface in combination with reduced damaging effect of coke deposition on catalyst surface and blocking of pores. Coke deposition on purely microporous catalysts causes more effective catalyst deactivation. In the case of the alumina sample, the strong deactivation was associated with the presence of Lewis acid sites that favored the formation of coke. The good glycerol conversion observed for MCM-36 and ITQ-2 therefore illustrates the advantages of combining Brønsted acid sites and mesoporosity.

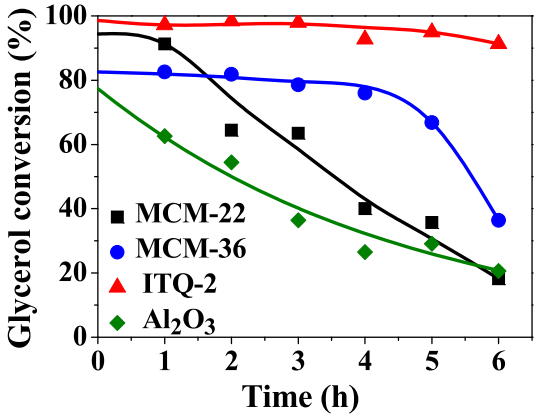

Fig. 5. Glycerol conversion for the different samples as a function of time.

The main reaction product obtained during glycerol dehydration was acrolein, and minor products were acetaldehyde, allyl alcohol, 3-hydroxypropanal, propionic acid, and heavily coked compounds, verified in Fig. 6 through the missing carbon balance of $[1 - C_{out}/C_{in}]$ outflowing the reactor. The very low carbon balance during the catalytic reaction and the black appearance of the used catalysts suggested the significant formation of coke, which negatively influenced the selectivity toward acrolein. After 6 h of reaction, the carbon balance reached the maximum value of 100% for the MCM-22 and MCM-36 catalysts, due to the low conversion. However, the ITQ-2 catalyst remained highly active, with a carbon balance of around 40% indicating that this catalyst had a much longer lifetime. Kubička et al. claim that as the zeolite channels are quickly blocked with carbonaceous compounds during the dehydration, the reaction occurs mainly in the exposed surface [3] and this can explain the higher ITQ-2 conversion.

Fig. 6 also reveals that the rate of coke formation diminishes during the dehydration reaction on MCM-22, as the carbon balance reaches 100% after 6 h on stream. Curiously, the selectivity to acrolein increases constantly and reaches almost 80%. The reason is that coke is formed preferentially on acid sites that deactivate intensively due to pore blockage on MCM-22. On the other hand, ITQ-2 is highly active even after 6 h, because of the different spatial location of the active sites [29].

Quantification of coke formation during the reaction was based on thermogravimetric analysis (Table 2). Considering the range of temperature between 400 and 650 °C, related to the loss of non-volatile carbonaceous byproducts, the MCM-22 zeolite showed a weight loss of 18.5%, while under the same conditions, the MCM-36 and ITQ-2 catalysts showed losses of 27.6 and 22.2%, respectively. Therefore, despite of the beneficial behavior of mesopores to acid sites accessibility and greater catalyst lifetime, it also contributes to form small domains between the exfoliated layers for coke storage

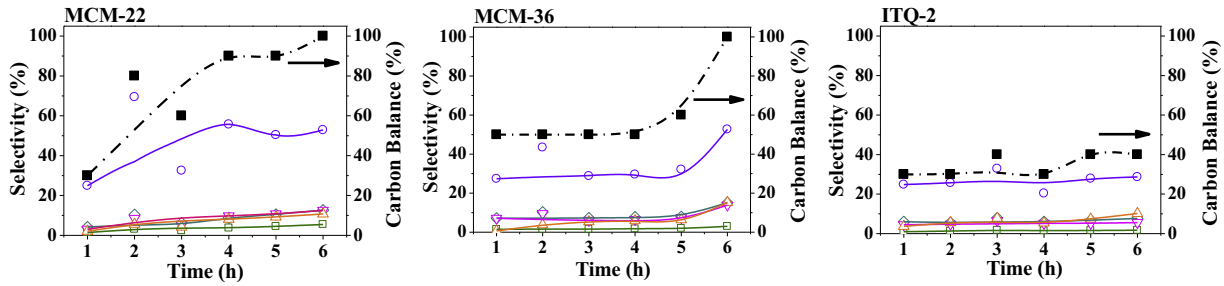

Fig. 6. Selectivity of products and carbon balance of the catalysts during glycerol dehydration; ◯ acrolein; ◊ acetaldehyde; □ allyl alcohol; △ propionic acid; ▽ 3-hydroxypropanal and ■ carbon balance.

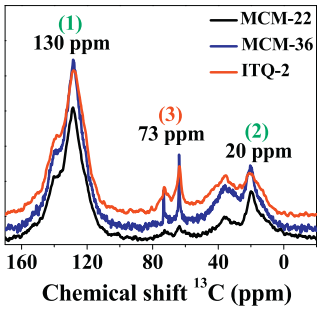

Fig. 7. ^{13}C NMR spectra of the spent catalysts, peaks numbered 1, 2 and 3 are assigned in Scheme 1.

Table 2
Catalyst deactivation after 6 h of reaction, and coke weight percentage.

Samples	Deactivation after 6 h (%)	Coke wt.%[a]
MCM-22	80.7	18.5
MCM-36	55.9	27.6
ITQ-2	7.3	22.2
Al_2O_3	82.7	45.0

[a] Weight loss determined by thermogravimetric analysis in the range of temperature between 400 and 650 °C.

[29]. In comparison to MCM-22, the single textural characteristics of MCM-36 and ITQ-2 cause a change in coke location essentially from micro to mesopores, thus avoiding a premature deactivation by blocking of pores. In the case of purely microporous zeolites, the coke is essentially deposited within external micropores and its effect on catalytic performance is more pronounced, even for low coke content, due to pore blockage and obstruction of the access of glycerol to narrow channels located deep in the crystals. However, in the case of mesoporous zeolites, the coke is preferentially located between the zeolite sheets, facilitating the retention of coke molecules in non-confined environments.

With the aid of ^{13}C NMR spectroscopy in Fig. 7, we could detect changes in the chemical composition of heavy molecules deposited on catalysts surface after 6 h on glycerol stream. The liquid ^{13}C NMR spectrum of glycerol (not shown) had very thin peaks well matched to the high mobility of glycerol molecules. On the other hand, the spectra of the spent catalysts had broadened peaks equivalent to bulky and less moveable organic molecules. The ^{13}C NMR spectra confirmed the changes in the nature and amount of carbonaceous deposits adsorbed on the spent catalysts. Two families of coke deposits named as aromatic and polyglycol were identified. The peak at δ = 130 ppm (peak 1 in Fig. 7) were attributed to carbon atoms in polyaromatic compounds, and peaks at δ = 19 and 35 ppm (peak 2) associated with saturated carbon atoms of terminal chains bounded to the oligomeric compounds that had not yet cyclized. The peaks at δ = 63 and 70 ppm were attributed to polyglycol compounds (branched oxygen-containing carbonaceous deposits, peak 3 in Fig. 7). The same behavior and signature of coke derived from glycerol conversion was detected in a previous publication [34].

In a preceding study [34] the suggested steps of polyaromatic accumulation involved the establishment of highly active monomeric species during the glycerol dehydration, followed by their transport and oligomerization inside the zeolite pores. This type of coke is more damaging for zeolites performance because the micropores are blocked with coke and obstructing the internal active sites causing a loss in conversion as sketched in Scheme 1. In contrast, the steps of polybranched ether molecules development involved the intermolecular dehydration of glycerol molecules activated on adjacent acid sites, followed by the successive coupling of hydroxyl groups of glycerol [34,35]. The formation of polyglycol molecules involved the transport of bulky polycondensed molecules, and, therefore occurred favorably on the external surfaces of the zeolites crystals, mainly in exposed sheets of modified zeolites noticeable in ^{13}C NMR.

Based on the results of glycerol conversion with time, thermogravimetric quantification of coke and on NMR spectroscopy, we

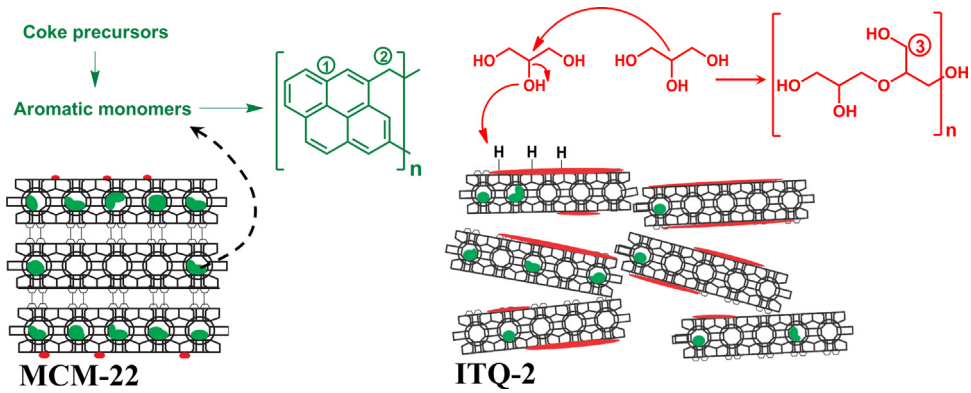

Scheme 1. Schematic picture of the zeolites deactivation during glycerol dehydration.

have sketched a microscopic picture of coke distribution on MCM-22 and ITQ-2 in Scheme 1. According to this scheme the two families of coke coexist, however they can grow predominantly in one environment or another depending on the textural properties of the zeolites. In purely microporous MCM-22 zeolite most of the coke are of polyaromatic molecules and peak 3 in Fig. 7 is almost absent, but the higher the external surface area of zeolites, the more abundant the polyglycols are.

4. Conclusions

The glycerol dehydration reaction was used to investigate aspects of the accessibility of MWW zeolites, considering changes in acidity and the resistance to coke formation. The zeolites modified by delamination and pillaring showed low acidity compared to MCM-22, although the increase in accessibility was advantageous for glycerol dehydration. The MCM-22 zeolite deactivated rapidly due to the blocking of micropores and making the internal channels inaccessible, which inhibited the reaction. The ITQ-2 zeolite showed higher conversion than the other zeolites, which could be explained by its greater accessibility. All the zeolites showed high selectivity toward acrolein (the desired product), which was maintained for up to 6 h reaction, despite deactivation, showing that the formation of coke and acrolein occurred at different acid sites.

The presence of mesopores in the modified zeolites was important in terms of both accessibility as well as coke deposition, avoiding blockage of all the micropores and channels. The formation of polyglycols was associated with the exposed surfaces of the materials, occurring preferentially for the MCM-36 and ITQ-2 zeolites, while the formation of polyaromatics was favored in the case of the microporous MCM-22 zeolite.

Acknowledgements

This work was supported by the Brazilian agencies CNPq (470094/2013-3) and FAPESP (project numbers 2010/01449-3, 2012/08305-2, 2013/01328-0 and 2013/08541-0).

References

[1] B. Katryniok, S. Paul, F. Dumeignil, ACS Catal. 3 (2013) 1819–1834.
[2] S.D. Blass, R.J. Hermann, N.E. Persson, A. Bhan, L.D. Schmidt, Appl. Catal. A: Gen. (2014) 10–15.
[3] D. Kubička, I. Kubičkova, J. Čejka, Catal. Rev. 55 (2012) 1–78.
[4] A. Witsuthammakul, T. Sooknoi, Appl. Catal. A: Gen. 413–414 (2012) 109–116.
[5] H. Serafim, I.M. Fonseca, A.M. Ramos, J. Vital, J.E. Castanheiro, Chem. Eng. J. 178 (2011) 291–296.
[6] B.O.D. Costa, M.A. Peralta, C.A. Querini, Appl. Catal. A: Gen. 472 (2014) 53–63.
[7] Y.T. Kim, K.D. Jung, E.D. Park, Appl. Catal. B: Environ. 107 (2011) 177–187.
[8] W.J. Roth, D.L. Dorset, Microporous Mesoporous Mater. 142 (2011) 32–36.
[9] W.J. Roth, P. Nachtigall, R.E. Morris, J. Čejka, Chem. Rev 114 (2014) 4807–4837.
[10] J.D. Rimer, M. Kumar, R. Li, A.I. Lupulescu, M.D. Oleksiak, Catal. Sci. Technol. 4 (2014) 3762–3771.
[11] F.S.O. Ramos, M.K. Pietre, H.O. Pastore, RSC Adv. 3 (2013) 2084–2111.
[12] W.J. Roth, P. Chlubna, M. Kubu, D. Vitvarova, Catal. Today 204 (2013) 8–14.
[13] U. Diaz, ISRN Chem. Eng. 2012 (2012) 35.
[14] W.J. Roth, B. Gil, B. Marszalek, Catal. Today 227 (2014) 9–14.
[15] W.J. Roth, J. Čejka, Catal. Sci. Technol. 1 (2011) 43–53.
[16] T. Selvam, A. Inayat, W. Schwieger, Dalton Trans. 43 (2014) 10365–10387.
[17] J. Wang, S. Jaenicke, G.K. Chuah, W. Hua, Y. Yue, Z. Gao, Catal. Commun. 12 (2011) 1131–1135.
[18] V. Machado, J. Rocha, A.P. Carvalho, A. Martins, Appl. Catal. A: Gen. 445–446 (2012) 329–338.
[19] U. Díaz, A. Corma, Dalton Trans. 43 (2014) 10292–10316.
[20] G. Belussi, A. Carati, C. Rizzo, R. Millini, Catal. Sci. Technol. 3 (2013) 833–857.
[21] A. Corma, V. Fornés, J. Martinez-Triguero, S.B. Pergher, J. Catal. 186 (1999) 57–63.
[22] A. Corma, U. Diaz, V. Fornés, J.M. Guil, J. Martínez-Triguero, E.J. Creyghton, J. Catal. 191 (2000) 218–224.
[23] A.L.S. Marques, J.L.F. Monteira, H.O. Pastore, Microporous Mesoporous Mater. 32 (1999) 131–145.
[24] A. Lacarriea, F. Luckb, D. Swierczynski, F. Fajulaa, V. Hulea, Appl. Catal. A: Gen. 402 (2011) 208–217.
[25] A. Corma, V. Fornes, S.B. Pergher, T.L.M. Maesen, S.G. Buglass, Nature 396 (1998) 353–356.
[26] A. Corma, V. Fórnes, J.M. Guil, S. Pergher, T.L.M. Maesen, J.G. Buglass, Microporous Mesoporous Mater. 38 (2000) 301–309.
[27] W.J. Roth, C.T. Kresge, J.C. Vartuli, M.E. Leonowicz, A.S. Fung, S.B. McCullen, Stud. Surf. Sci. Catal. 94 (1995) 301–308.
[28] C.A. Emeis, J. Catal. 141 (1993) 347–354.
[29] L.G. Possato, R.N. Diniz, T. Garetto, S.H. Pulcinelli, C.V. Santilli, L. Martins, J. Catal. 300 (2013) 102–112.
[30] A. Zukal, M. Kubú, Dalton Trans. 43 (2014) 10558–10565.
[31] B. Gil, W. Makowski, B. Marszalek, W.J. Roth, M. Kubu, J. Čejka, Z. Olejniczak, Dalton Trans. 43 (2014) 10501–10511.
[32] J.A. van Bokhoven, N. Danilina, in: J. Čejka, A. Corma, S. Jones (Eds.), Zeolite and Catalysis Synthesis, Reactions and Applications, Wiley-VCH Verlag GmbH & Co. Inc., New York, 2009, pp. 281–304.
[33] M.J. Duer, Solid-State NMR Spectroscopy Principles and Applications, 1st ed., Blackwell Science Ltd., London, 2002.
[34] L.G. Possato, W.H. Cassinelli, T. Garetto, S.H. Pulcinelli, C.V. Santilli, L. Martins, Appl. Catal. A: Gen. 492 (2015) 243–251.
[35] M. Guisnet, P. Magnoux, Appl. Catal. 54 (1989) 1–27.